








Image analysis of volcanic plumes: A simple calibration tool to correct for the effect of wind

 Eveanjelene Snee^α,  Paul A. Jarvis^{*β,γ},  Riccardo Simionato^{γ,δ},  Simona Scollo^ε,
 Michele Prestifilippo^ε,  Wim Degruyter^α, and  Costanza Bonadonna^γ

^α School of Earth and Environmental Sciences, Cardiff University, Main Building, Park Place, Cardiff, CF10 3AT, UK.

^β GNS Science, PO Box 30368, Lower Hutt 5040, New Zealand.

^γ Department of Earth Sciences, University of Geneva, Rue des Maraichers 13, 1205, Geneva, Switzerland.

^δ Dipartimento di Geoscienze, Facoltà di Scienze, Università degli Studi di Padova, 35131 Padova, Italy.

^ε Istituto Nazionale di Geofisica e Vulcanologia, Osservatorio Etneo, 95125, Catania, Italy.

ABSTRACT

Video cameras provide vital information on volcanic plumes from explosive eruptions, such as plume height, for monitoring and research. These images must be calibrated to get accurate quantitative data. However, the presence of wind complicates any calibration as the plume may no longer lie in the image plane, i.e. a plane perpendicular to the camera's line-of-sight. Here, we present a simple new tool to correct for the effect of wind on the position and height of a volcanic plume as determined from imagery by rotating the image plane to be in the direction of the wind. We show the importance of accounting for the effect of wind on the maximum plume height determined from videos for two case-studies; a Vulcanian explosion from Sabancaya volcano, Peru, and a sustained plume from Mount Etna, Italy. This tool can improve the accuracy of quantitative information extracted from images of volcanic plumes, and should prove useful for both research and monitoring purposes.

KEYWORDS: Plume; Camera; Image analysis.

1 INTRODUCTION

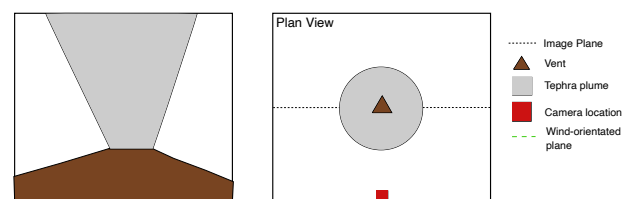
Videos of volcanic plumes significantly enhance the monitoring of volcanic eruptions. They are extensively used by volcano observatories around the world, e.g. INGV-OE, Italy [Scollo et al. 2014; 2019], Alaska volcano observatory, USA, [Cameron et al. 2018], GNS, New Zealand, [Miller and Jolly 2014] and many more, to monitor eruption style, activity level and eruption characteristics in real-time. Additionally, recorded videos of volcanic plumes, in both visible and thermal wavelengths, can be used for improving our understanding of volcanic eruptions [Sparks and Wilson 1982; Formenti et al. 2003; Patrick 2007; Sahetapy-Engel and Harris 2009; Harris et al. 2013; Webb et al. 2014; Tournigand et al. 2017], as well as providing important data sources for the validation of eruption models [Terada and Ida 2007; Suwa et al. 2014]. In all of these situations, an important quantity of interest is the height of the volcanic tephra plume, a key parameter used to help constrain the source conditions of an eruption and an input parameter for ash dispersal forecasting [Bonadonna et al. 2012; Folch 2012; Scollo et al. 2014; 2019; Dioguardi et al. 2020].

To extract any quantitative information from an image of a volcanic plume, such as plume height, the camera image has to be calibrated such that plume-containing pixels in the image can be associated with a physical location. A calibration can be applied by using trigonometry, considering the camera set up (orientation and inclination) and assuming that the plume is within the image plane of interest [Bombrun et al. 2018], which is defined as the vertical plane perpendicular to the camera orientation that passes through the vent. However, volcanic plumes are affected by atmospheric wind [Bur-

sik 2001; Degruyter and Bonadonna 2012; Dürig et al. 2021] and therefore may not always lie in the image plane. Figure 1 highlights this problem. When the plume is strong, it is not significantly impacted by the wind and lies within the image plane at all heights above the vent. But when the plume is weak and heavily impacted by the wind, the plume diverges from the assumed image plane. Despite this complexity, only a few camera calibrations for volcanic plumes include the effect of wind [e.g. Scollo et al. 2014].

In this paper, we present a free, easy-to-use tool that can be used to calibrate images of volcanic tephra plumes. This

Strong Plume - No Wind



Weak Plume - Wind affected

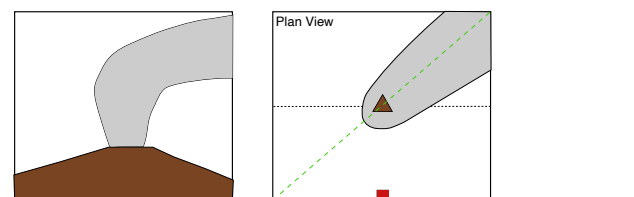


Figure 1: Schematic showing how a plume lies on the assumed image plane when the plume is strong compared to when the plume is impacted by the wind and does not lie on the image plane.

*✉ p.jarvis@gns.cri.nz

tool, called `windyPlume` and available in MATLAB and Python (see [Data Availability](#) section), allows for the user to input their camera properties, weather data, and the pixels to be calibrated to determine the heights of these points above sea level. The horizontal distances between the points of interest and the camera are also calculated. We demonstrate the application of this package to two different styles of volcanic activity, a Vulcanican explosion and a sustained tephra plume, from Sabancaya volcano, Peru, and Mount Etna, Italy, respectively. Both examples show the importance of considering the effect of wind on the height calculation of wind-affected plumes. We consider the suitability of this approach to different styles of explosive eruptions, as well as consider the associated uncertainties.

2 METHOD

Before describing the methodology, we first need to summarise the underlying assumptions that underpin the method. The principle assumption is that the plume is contained within a vertical plane that passes through the volcanic vent and whose orientation is controlled by the wind direction [Scollo et al. 2014]. We refer to this as the wind-oriented plane (Figure 1). This assumption implicitly involves approximating the three-dimensional plume as a two-dimensional slice. Furthermore, this also requires the definition of a single wind direction, neglecting variations with both time and altitude. The wind direction can be chosen through analysis of data from nearby weather stations (i.e. atmospheric soundings*), or from ECMWF Reanalysis data [Berrisford et al. 2011; Dee et al. 2011; Hersbach et al. 2020].

In addition to the wind-oriented plane, it is necessary to consider a second plane, here referred to as the image plane (Figure 1), which is defined as a vertical plane passing through the volcanic vent but perpendicular to the horizontal projection of the line-of-sight (LOS) of the camera. The camera sees a projection of the volcanic plume onto this plane. Unless the wind orientation is perpendicular to the horizontal LOS, the wind-oriented and image planes are not aligned. The wind calibration presented here, therefore, relates the physical location of the plume to its projected location within the image plane.

First, we use the image plane to define a right-handed Cartesian coordinate system where the origin is defined as the intersection of the LOS and the image plane. The y -axis is defined to be parallel to the horizontal projection of the LOS, with $y = 0$ defined by the image plane itself. Meanwhile, the z axis is vertically-aligned with $z = 0$ defined as the altitude of the camera. Finally, the x -axis is mutually-perpendicular to the others, in a horizontal orientation within the image plane.

We denote the spatial position of points in the wind-oriented plane using the vector coordinate $\mathbf{x} = (x, y, z)$. Meanwhile, we denote the projections of these points in the image plane by $\mathbf{x}' = (x', y' = 0, z')$, noting that $y = 0$ everywhere within the image plane. The purpose of the wind-corrected calibration is therefore to find the relationship between \mathbf{x} and \mathbf{x}' .

In addition to the relationship between \mathbf{x} and \mathbf{x}' , it is also necessary to relate physical locations in the image plane, given by \mathbf{x}' , to pixel locations in the image. For this part of the calibration, we adapt the methodology of Bombrun et al. [2018] and make use of the camera inclination ϕ , the vertical and horizontal field of views (FOVs), θ_v and θ_h , respectively, and the perpendicular distance between the camera and the image plane d . Note that throughout this paper all angles are measured in degrees. Whilst the camera properties ϕ , θ_v and θ_h should ideally be recorded at the time of image capture, we also present example strategies of how to estimate these afterwards in Appendix A.

2.1 Image plane calibration

Figure 2 demonstrates how ϕ , θ_v , θ_h , and d can be used to relate the positions of individual pixels within the image to \mathbf{x}' . We define the pixel position as (i, j) , with i the i^{th} pixel as measured from the left of the image, and j the j^{th} pixel as measured from the bottom. Furthermore, N denotes the number of pixels in the vertical direction and M the number of pixels in the horizontal. Following Bombrun et al. [2018], the physical height of the j^{th} pixel in the image plane is given by

$$z'(j) = \frac{d}{2} \left[\tan \left(\phi - \frac{\theta_v}{2} + (j-1)\delta\theta_v \right) + \tan \left(\phi - \frac{\theta_v}{2} + j\delta\theta_v \right) \right], \quad (1)$$

where $\delta\theta_v = \theta_v/N$ is the vertical angle subtended by an individual pixel. Similarly, the physical horizontal location of the i^{th} pixel in the image plane is given by

$$x'(i) = \frac{d}{2} \left[\tan \left(-\frac{\theta_h}{2} + (i-1)\delta\theta_h \right) + \tan \left(-\frac{\theta_h}{2} + i\delta\theta_h \right) \right], \quad (2)$$

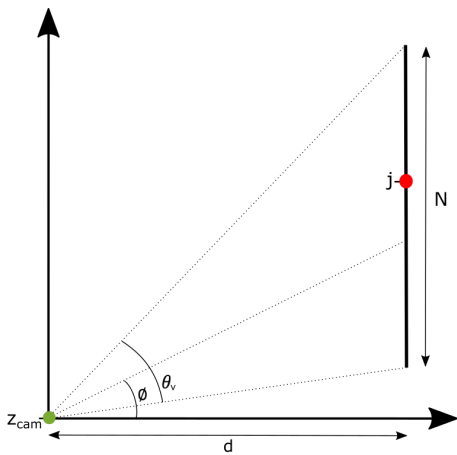
where $\delta\theta_h = \theta_h/M$ is the horizontal angle subtended by an individual pixel. Note that, in Equation 2, the position $x' = 0$ is taken to be the centre of the image. Positions with respect to the left hand side of the image can be obtained with the transformation $x' \rightarrow x' + d \tan(\theta_h/2)$ [Simionato et al. 2022].

2.2 Projection between image and wind-oriented planes

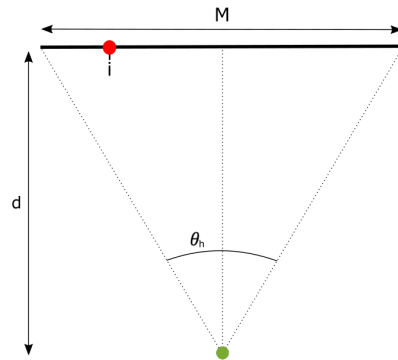
In order to calculate the projection relating \mathbf{x} and \mathbf{x}' , it is necessary to find the vector $\Delta\mathbf{x} = (\Delta x, \Delta y, \Delta z)$, such that $\mathbf{x} = \mathbf{x}' + \Delta\mathbf{x}$. The precise expressions for the components of $\Delta\mathbf{x}$ vary according to the relative orientations of the image and wind-oriented planes, and whether \mathbf{x}' is to the left or right of the vent in the image. Here, we will present a derivation of the projection for the case that the wind oriented plane goes between the top left and bottom right quadrants of the coordinate system defined by the image plane, and that \mathbf{x}' is to the left of the vent. The equivalent expressions for other scenarios can be derived in an entirely analogous fashion and are presented in Table 1.

* <http://weather.uwyo.edu/upperair/sounding.html>

Vertical Geometrical Calibration



Horizontal Geometrical Calibration



- Horizontal distance d between camera and reference
- M Width of image frame in pixels
- N Height of image frame in pixels
- j Pixel number as measured from the bottom
- i Pixel number as measured from the left
- θ_v Field of view (vertical)
- θ_h Field of view (horizontal)
- ϕ Inclination
- Point to calibrate
- Camera

Figure 2: Sketch showing the parameters used to relate physical location of points in the image plane $\mathbf{x}' = (x', z')$ to the pixel location in the image (i, j) . Parameters defined as ϕ = camera inclination, θ_v = vertical field of view (FOV), θ_h = horizontal FOV, d = perpendicular distance from camera to image plane, M = image width in pixels, N = image height in pixels.

Table 1: The equations for the correction to the geometrical calibration due to wind, where λ is the acute angle between wind direction and image plane, $\alpha = i\delta\theta_h$ and $\chi = j\delta\theta_v$. The schematics in the first column show the wind orientation (double ended arrow) with respect to the the image plane (solid line). The green dot denotes the camera position.

Wind direction in the image	h	x' to the right of the vent	x' to the left of the vent
	$\frac{b \sin(\lambda)}{\cos(\alpha - \frac{\theta_h}{2} - \lambda)}$	$\Delta x = h \sin\left(\frac{\theta_h}{2} - \alpha\right)$ $\Delta y = -h \cos\left(\frac{\theta_h}{2} - \alpha\right)$ $\Delta z = \Delta y \tan\left(\phi - \frac{\theta_v}{2} + \chi\right)$	$\Delta x = -h \sin\left(\frac{\theta_h}{2} - \alpha\right)$ $\Delta y = h \cos\left(\frac{\theta_h}{2} - \alpha\right)$ $\Delta z = \Delta y \tan\left(\phi - \frac{\theta_v}{2} + \chi\right)$
	$\frac{b \sin(\lambda)}{\cos(\alpha - \frac{\theta_h}{2} + \lambda)}$	$\Delta x = -h \sin\left(\frac{\theta_h}{2} - \alpha\right)$ $\Delta y = h \cos\left(\frac{\theta_h}{2} - \alpha\right)$ $\Delta z = \Delta y \tan\left(\phi - \frac{\theta_v}{2} + \chi\right)$	$\Delta x = h \sin\left(\frac{\theta_h}{2} - \alpha\right)$ $\Delta y = -h \cos\left(\frac{\theta_h}{2} - \alpha\right)$ $\Delta z = \Delta y \tan\left(\phi - \frac{\theta_v}{2} + \chi\right)$

Figure 3A shows a bird’s-eye view of how the projection from \mathbf{x} to \mathbf{x}' is calculated for this initial scenario whilst Figure 3B shows the triangle formed by the volcanic vent, \mathbf{x} and \mathbf{x}' in more detail. Using the sine rule, followed by the angle addition formula, as well as $\sin(90^\circ) = 1$ and $\cos(90^\circ) = 0$, the horizontal distance between \mathbf{x} and \mathbf{x}' can be expressed as

$$h = \frac{b \sin(\lambda)}{\sin\left(90 - \frac{\theta_h}{2} + \alpha - \lambda\right)} = \frac{b \sin(\lambda)}{\cos\left(\alpha - \frac{\theta_h}{2} - \lambda\right)}, \quad (3)$$

where $b = |\mathbf{x}' - \mathbf{x}'_v|$, λ is the acute angle between the image and wind-oriented planes, $\alpha = i\delta\theta_h$ and \mathbf{x}'_v is the horizontal position of the vent in the image plane. Then, using Pythagoras’ theorem, and the same trigonometric identities as before, it is possible to find the x -component of the separation between \mathbf{x} and \mathbf{x}' to be

$$\Delta x = h \cos\left(90 - \frac{\theta_h}{2} + \alpha\right) = -h \sin\left(\frac{\theta_h}{2} - \alpha\right). \quad (4)$$

In an analogous fashion, the y -component of separation can be seen to be given by

$$\Delta y = h \sin\left(90 - \frac{\theta_h}{2} + \alpha\right) = h \cos\left(\frac{\theta_h}{2} - \alpha\right). \quad (5)$$

Finally, Figure 4 shows a side view of how Δy , together with the previously defined quantities, can be used to define the vertical distance between \mathbf{x} and \mathbf{x}' , which is given by

$$\Delta z = \Delta y \tan\left(\phi - \frac{\theta_v}{2} + \chi\right), \quad (6)$$

where $\chi = j\theta_v/N$. With equations 4 to 6, it is therefore possible to completely calculate \mathbf{x} from \mathbf{x}' .

A final consideration is that the position \mathbf{x} is relative to the origin of the coordinate system defined above, i.e. the intersection of the horizontal projection of the camera LOS and the image plane. Therefore, values of z are relative to the altitude of the camera, and must be adjusted to obtain heights above the vent or sea-level as desired. Similar adjustments must be

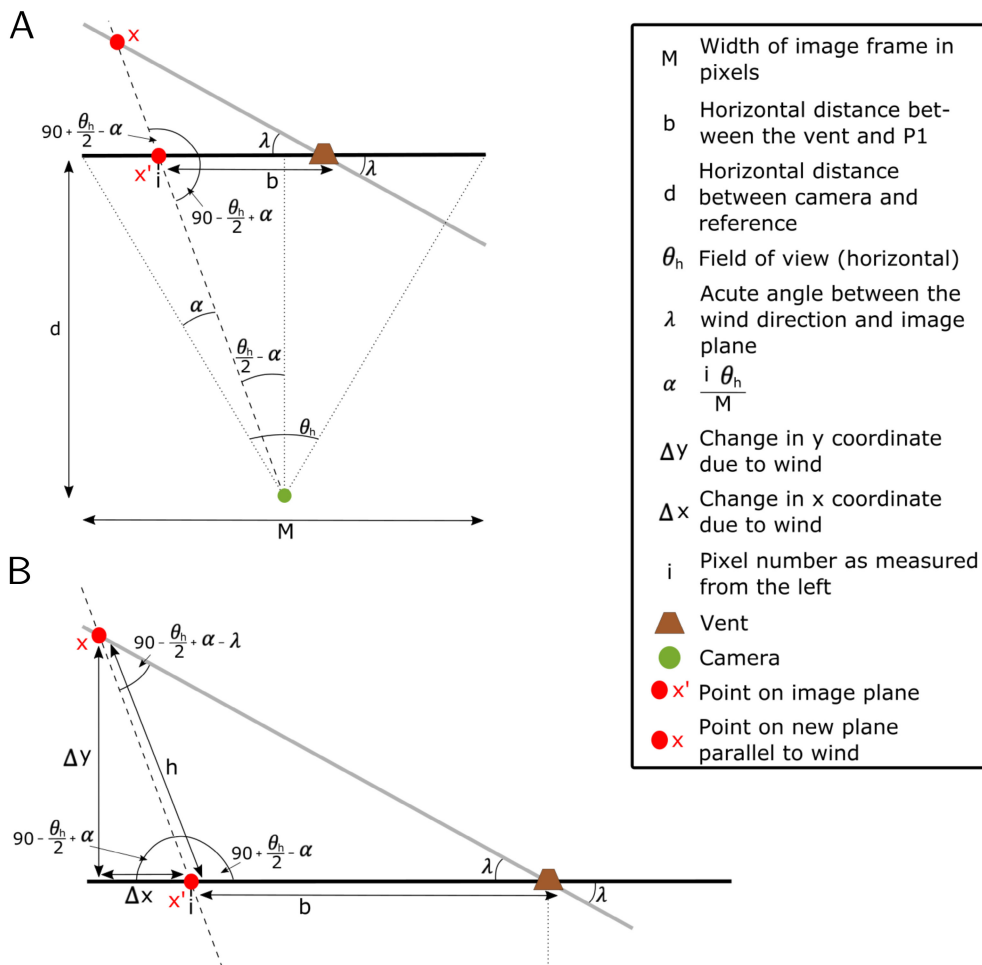


Figure 3: Diagram defining the length and angles used to apply the wind correction to determine the horizontal change in position. [A] shows a bird's-eye view of the whole region of interest and [B] shows the triangle formed by x , x' and the vent in more detail.

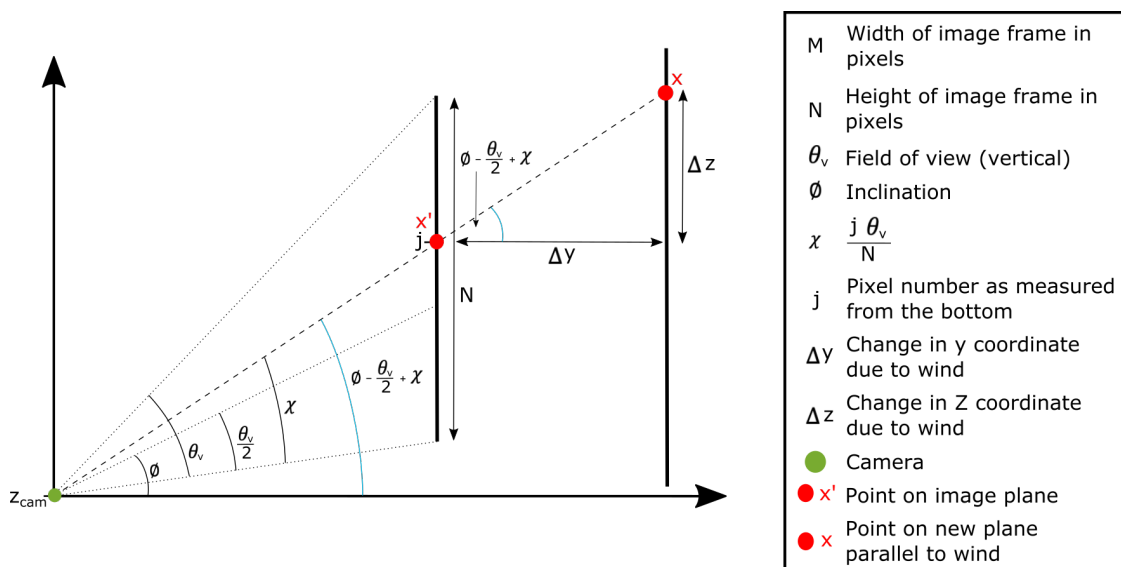


Figure 4: Diagram of a side-view defining the length and angles used to apply the wind correction to determine the vertical change in position.

made to x and y to obtain the horizontal distance of a point from the vent.

3 CASE STUDIES

3.1 Sabancaya volcano, Peru

Sabancaya volcano, Peru, is a stratovolcano in the Central Volcanic Zone. Since November 2016, it has been producing multiple Vulcanian explosions daily [Kern et al. 2017; Manrique Llerena et al. 2018; Coppola et al. 2022]. Video S1 in the [Supplementary Material](#) shows one such Vulcanian explosion that occurred at 14:47 UTC on 31 July 2018. The original video was recorded at 50 fps, but has been resampled to 1 fps and accelerated by a factor of 10. It can clearly be seen that the generated plume is strongly wind-affected. [Figure 5A](#) shows the relative locations of the vent and camera used to capture the video. The properties related to the camera used to capture the video can be found in [Table 2](#). The camera line of sight was orientated along a bearing of $\omega = 350^\circ$ whilst, for this particular video, $\theta_h = 64^\circ$ (see [Appendix A](#)). These values can be used to define the image plane (dashed-line) as described in [Section 2](#).

The wind-oriented plane has been determined from ERA5 hourly reanalysis data [Hersbach et al. 2018]. Specifically, we extract the vertical profiles of geopotential and East- and North-components of wind velocity at different pressure levels at the closest time (15:00 UTC) to the explosion and closest location (latitude = -15.75° , longitude = -71.75°) to the vent from the database of [Hersbach et al. 2018](#). The two components of velocity can be used to calculate the wind direction, presented in [Figure 5B](#) as a bearing from North and as a function of altitude. In order to define a unique wind direction to use for the calibration procedure, we find the average wind direction over the 4 km above the vent to be 110° , with a standard deviation of 20° . We choose 4 km as the upper limit to this range since it is slightly greater than the wind-uncorrected height, and we will justify *a posteriori* that this remains more than the final wind-corrected height reached by the plume.

Now that both the image and wind-oriented planes have been defined, it is possible to calculate that, in this case, $\lambda = 30^\circ$. This information is sufficient to calculate the wind correction ([Table 1](#)). Firstly, a wind-uncorrected plume height time-series is determined following the image analysis procedure presented in [Simionato et al. 2022](#) and the geometric calibration described in [Section 2.1](#) [Bombrun et al. 2018]. The wind calibration ([Section 2.2](#)) is then performed. [Figure 6](#) shows a time series of the plume height calculated both with and without the wind-correction. It can be seen that neglecting the effect of the wind can lead to an over-estimation of the plume height by up to about 50 %. Thus, when using visible images to characterise wind-affected Vulcanian plumes, it is important to account for the effect of wind.

3.2 Mt. Etna volcano, Italy

Mount Etna, on the Italian island of Sicily, is one of the most active volcanoes in the world. It regularly produces tephra plumes during paroxysmal eruptions, that have reached heights of up to 15 km a.s.l [Vulpiani et al. 2016; Corradini et al. 2018]. One such example is the 12 April 2013 eruption. The climactic phase of this eruption began at 11:02:22 UTC and finished at 11:59:12 UTC [Freret-Lorgeril et al. 2018]. During this

phase, a weak wind-affected eruption column from the South East Crater was produced [Scollo et al. 2019]. Recordings of this eruption were captured by the operational monitoring webcams of the Istituto Nazionale di Geofisica e Vulcanologia - Osservatorio Etneo (INGV-OE) and, here, we focus on the calibration of the webcam that is located in the city of Catania (ECV camera) [Calvari et al. 2011; 2018]. The relative locations of the vent and camera used to capture the images can be seen in [Figure 7a](#). The camera LOS was orientated along a bearing of $\omega = 351.5^\circ$, whilst θ_h is determined to be 18° (see [Appendix A](#)). These values can be used to define the image plane (dashed-line, [Figure 7](#)) as described in [Section 2](#). Additional camera properties (e.g. camera image size, inclination of the camera) can be found in [Table 2](#).

To determine the position of the wind-oriented plane, the wind orientation is determined from ECWMF reanalysis data [Berrisford et al. 2011; Dee et al. 2011]. Specifically, the vertical profiles of geopotential and East- and North-components of wind velocity at different pressure levels above the summit region (latitude = 37.748° , longitude = 14.999° *) and times associated with specific images are used. As with the previous case-study of Sabancaya, the eastward- and northward components of the horizontal wind velocity, u_E and u_N , respectively, are used to determine the wind direction as a bearing from North ([Figure 7B](#)). Furthermore, the unique wind direction to use for the calibration procedure is defined as the average wind direction over 12 km above the vent, and found to be in the range $100\text{--}104^\circ$ for all the different times examined. 12 km is chosen as the upper limit of this range since this is generally the plausible height that tephra plumes from paroxysmal eruptions reach, however it is worth noting that they have been recorded to go higher [Vulpiani et al. 2016; Calvari et al. 2018; Corradini et al. 2018]. As the image and wind-oriented planes have now been determined, λ can now be calculated as 19° (for the average wind orientation above the vent for all times), and the calibration can now be applied to produce a calibrated plume height time-series.

The calibrated plume height time-series for this eruption can be seen in [Figure 8](#). The maximum plume height was determined automatically in MATLAB by first subtracting the red channel from the blue channel, and then detecting the highest location in the frame where 10 vertically connected pixels all have a pixel intensity value less than 0.2 [Snee 2021]. This plume height time-series in pixels is then calibrated with the geometrical calibration ([Section 2.1](#), [Bombrun et al. \[2018\]](#)) to produce a wind-uncorrected plume height time-series ([Figure 8](#), solid black line). The wind calibration ([Section 2.2](#)) is then performed ([Figure 8](#), dashed golden line). A comparison between the wind-uncorrected and wind-corrected plume height time series shows that if wind is not considered, the maximum plume height would be overestimated for this eruption ([Figure 8](#)). However, as the original image plane and the wind-orientated plane are similar in orientation, the difference the wind-adjustment makes is relatively small. Therefore, as with the example of a Vulcanian plume from Sabancaya volcano, when using visible images to characterise wind-affected

*<https://volcano.si.edu/volcano.cfm?vn=211060>

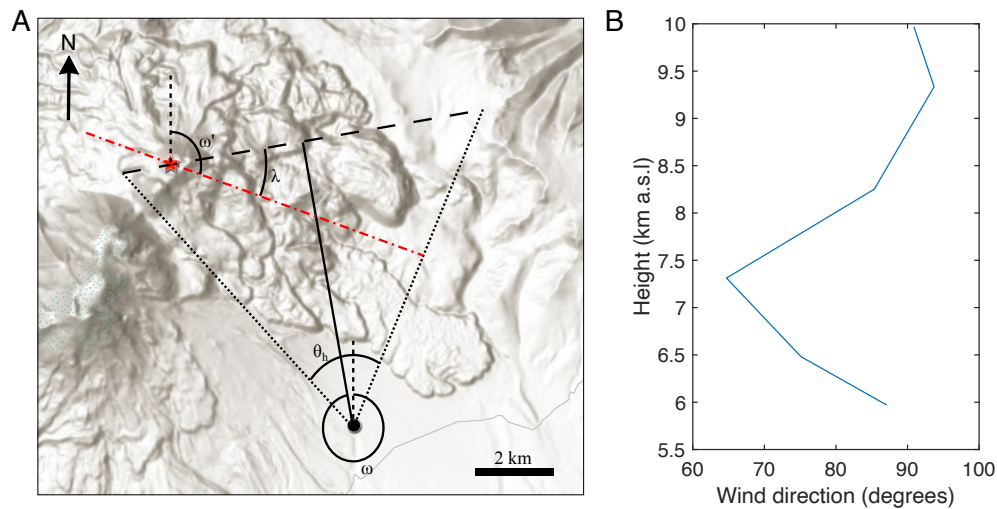


Figure 5: [A] Map showing relative locations of the Sabancaya vent (red star) and the camera (black circle). Additionally, the line of sight of the camera is shown by the solid black line, at a bearing of $\omega = 350^\circ$. The dotted lines demarcate the extent of the horizontal field of view $\theta_h = 64.3^\circ$. The image plane is therefore given by the dashed line. The red dotted-dashed line is the wind-oriented plane, at a bearing of $\omega' = 110^\circ$. Thus, the angle between the two planes $\lambda = 30^\circ$. [B] The wind direction measured as a bearing from North.

Table 2: Table of the camera properties used for each case study, where θ_H is the horizontal field of view, ϕ the inclination, ω the camera's line of sight and d the perpendicular distance between camera and image plane. See Appendix A for details of how θ_h and ϕ are calculated.

	Sabancaya	Mount Etna
Camera type	Canon Legria HF G40	Canon VC-C4R
Camera location	15.846S 71.814W	37.514N 15.044E
Camera height (m a.s.l.)	4561	137
Frame dimensions (pixels)	1920 × 1080	704 × 608
θ_H (°)	64	18
ϕ (°)	14	12
ω (°)	350	352
d (m)	7200	27 000

sustained plumes, it is important to account for the effect of wind.

4 DISCUSSION

4.1 Controls on magnitude of wind correction

The case studies in Section 3 show that the magnitude of the wind correction depends on the eruption in question. For example, at Mount Etna, where the wind direction is commonly perpendicular to the orientation of the ECV visible video camera, such that the wind-orientated and image planes nearly align, the wind correction is typically small. Indeed, for our specific case study of 12 April 2013, the magnitude of the wind correction is typically < 0.5 km (Figure 8). Additionally, the wind correction magnitude also increases with horizontal distance from vent. This is demonstrated in Figure 6, where we see that for the 31 July 2018 Sabancaya eruption, the size of

the wind correction grows to nearly 2 km as the plume moves horizontally away from the vent.

These two controls on the wind correction magnitude are depicted in Figure 9, which shows how the height obtained with the wind correction for four different points in an image from the ECV camera at Mount Etna varies with the wind orientation ω' . It can clearly be seen that, as $\omega' \rightarrow \omega$ (the camera orientation) or $\omega' \rightarrow \omega - 180^\circ$, the obtained height strongly depends on ω' . Thus, when the wind direction and camera orientation are close to parallel, the magnitude of the wind correction can become very large. Indeed, for such a configuration, small errors in the orientation can result in large errors in the calculated height. Figure 9 also shows that the difference between the heights obtained with and without the wind correction also increases with increasing horizontal distance from the volcanic vent (see, for example, the steeper gradient of the black line relative to the blue). Therefore, to

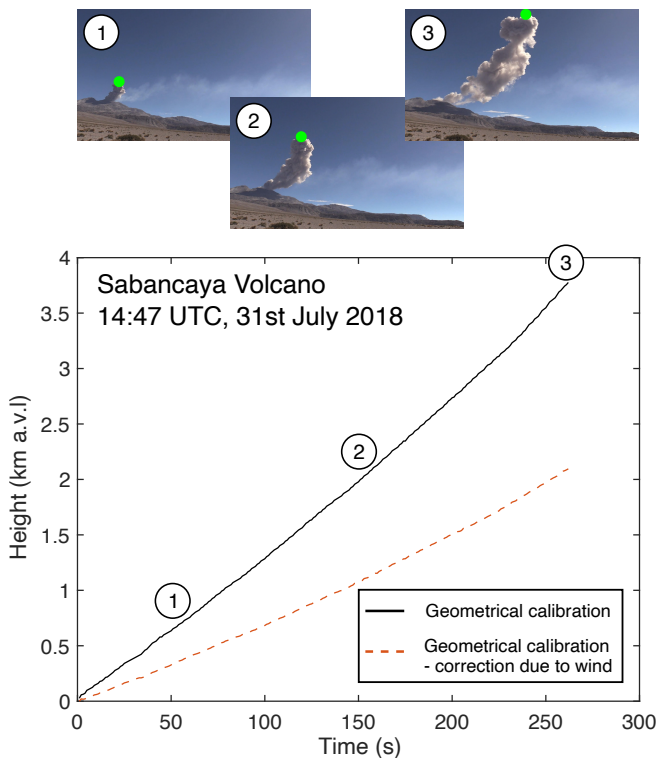


Figure 6: Plume height above the vent as a function of time when calculated with (red, dashed line) and without (solid black line) the wind-corrected calibration.

ensure the most accurate plume heights, the effect of wind on plume height estimates should be considered, particularly for plume tops close to the edge of the frame.

4.2 Limitations

Despite the advantages of this methodology, a number of limitations have to be considered. In particular, depending on the wind orientation and strength, camera orientation and eruption strength, there are circumstances when the calibration should not be applied. As highlighted by Figure 9, when the wind direction and camera orientation are parallel ($\omega' = \omega$ or $\omega' = \omega - 180$), the correction cannot be performed. Even if these two directions are only nearly parallel, the correction should not be performed. This is because a) the assumption that the plume is confined within the 2D image plane is no longer valid and b) the increased sensitivity on wind direction and camera orientation means small errors in these quantities can result in large errors in the wind-corrected height.

The wind correction should also not be applied to strong plumes, i.e. those that are approximately vertical. This is because the shape of strong plumes is not affected by the wind and, therefore, the point of maximum plume height may not lie within the wind-oriented plane. Some volcanic plumes, e.g. Cerro Negro, Nicaragua (9–12 April 1992), Hekla, Iceland (17 August 1980) [Carazzo et al. 2014], are neither strong nor weak and are often referred to as intermediate, transitional, or distorted plumes [Bonadonna et al. 2015]. In this case, it may not be appropriate to apply the wind correction on the eruptive column itself if it does not appear to be significantly wind-

affected. However, if the upper parts of the column and the horizontally spreading cloud are affected by wind, it may be reasonable to apply the correction here. The decision on when the wind correction should be applied can be challenging as it is difficult to numerically quantify whether a plume is intermediate or weak. Classification schemes for plume strength do exist [e.g. Degruyter and Bonadonna 2012], but the boundaries between strong, intermediate, and weak plumes of these classification schemes vary [Degruyter and Bonadonna 2012; Bonadonna et al. 2015; Scollo et al. 2019]. Therefore such scalings cannot currently be used as a way to automatically determine whether or not to apply the wind correction, nor can they inform the user on which part of the plume is wind affected as these scalings give a value for the plume as a whole. Additionally, further investigation would be needed to determine if a correlation does exist between these scalings and the applicability of the wind calibration. Therefore, currently, the user has to make a judgement as to where and when it is appropriate to apply the wind calibration.

Finally, temporal variations in the wind direction may create another set of conditions where it would be inappropriate to apply the calibration. Specifically, if the timescale over which the wind direction changes is shorter than or comparable to timescales of plume rise and/or the observation period then the obtained calibration is likely to be inaccurate. A user will therefore need to assess these timescales, as well as the magnitude of wind direction change, to assess if it is appropriate to apply to calibration. This is likely to be an issue for steady eruption plumes, such as the Mt Etna eruption in Section 3.2 rather than for short transient eruptions like at Sabancaya (Section 3.1). However, as shown in Figure 7, the wind direction varied very little during the observation period of the Mt. Etna case study.

4.3 Sources of uncertainty

A significant source of uncertainty in the wind calibration arises from knowledge of the wind field itself. In this study, we have estimated wind orientation from ERA-Interim [Berrisford et al. 2011; Dee et al. 2011] and ERA5 [Hersbach et al. 2018] reanalysis data. These have temporal resolutions of 12 and 1 hour(s), respectively, and therefore some form of interpolation is necessary to estimate the wind field at the time of eruption. Additionally, shorter-timescale perturbations to the wind field cannot be accounted for. Furthermore, the limits on horizontal spatial resolution also mean a spatial interpolation is required as well [Berrisford et al. 2011; Dee et al. 2011; Hersbach et al. 2018]. Alternative sources of weather data could include GNSS (Global Navigation Satellite System) soundings or local weather stations but all suffer from uncertainties associated with temporal and spatial resolutions. Moreover, in the case studies presented here, the wind orientation used is an average of the wind orientation above the vent up to a specified height. While this is necessary since the calibration uses only a single wind orientation, it is unrealistic as in reality the wind orientation changes with height. This technique of defining a unique wind orientation also requires the top height up to which the averaging takes place to be defined, which may be unknown and requires the user to estimate.

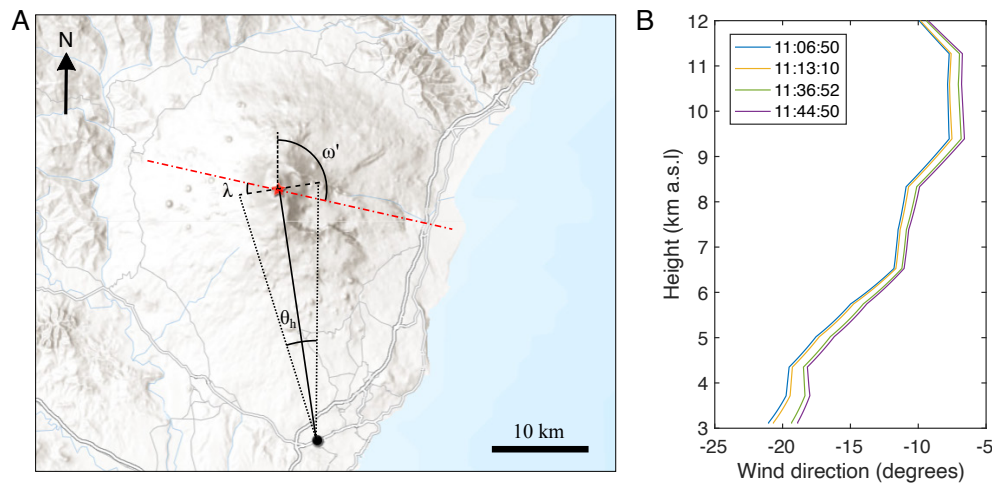


Figure 7: [A] Map showing the relative locations of the Mount Etna vent (red star) and the camera (black circle). The camera's line of sight is shown by the solid black line, at a bearing of $\omega = 351.5^\circ$. The dotted lines denote the extent of the horizontal field of view $\theta_h = 18^\circ$. The image plane is therefore given by the dashed line. The red dotted-dashed line is the wind-oriented plane, which here is drawn at a bearing of $\omega' = 102^\circ$. [B] The wind direction, measured as a bearing from North, as a function of altitude for different times during the eruption.

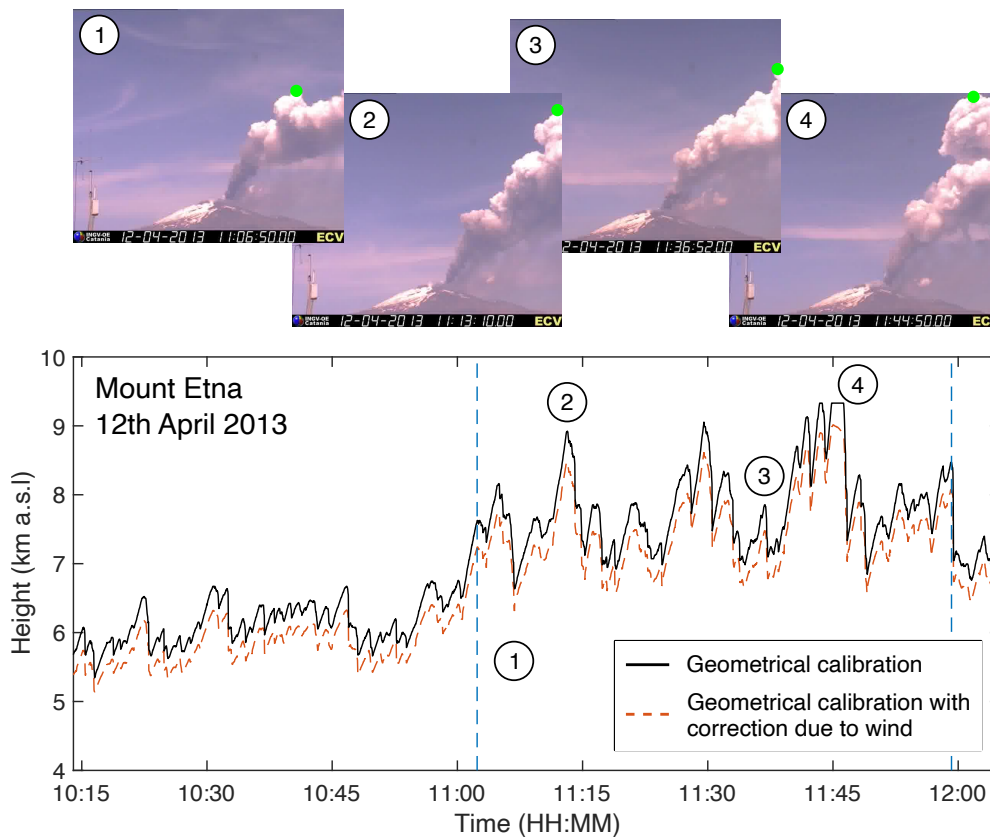


Figure 8: Time series of plume height for the Mount Etna case study, showing both the wind-corrected and wind-uncorrected measurements. The green circle in the images identifies the highest point of the plume.

However, for the two eruptions examined, the variability of the wind orientation above the vent with height is small; thus so is the uncertainty associated with it.

A further source of uncertainty can arise from inaccurate or imprecise knowledge of the properties of the camera used to image the eruption, specifically the field of view and the cam-

era orientation and inclination. Whilst such metadata should be recorded, there are challenges associated with this. Accurately and precisely measuring the inclination or orientation of off-the-shelf cameras is not always easy whilst cameras installed as part of a monitoring network can be moved by external factors such as birds or earthquakes. In [Appendix A](#),

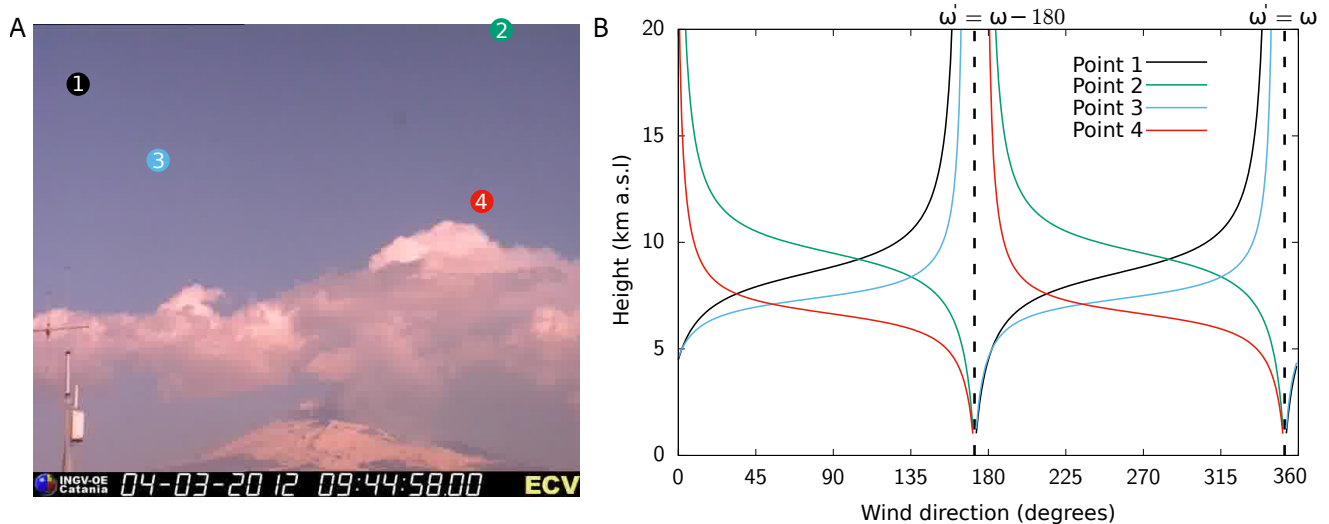


Figure 9: [A] Typical view from the ECV webcam at Mt. Etna, with four arbitrary points selected. [B] Dependence of the height of the selected points on wind direction.

we provide methods for how the camera field of view and inclination can be estimated if they are not known accurately, relying on knowledge of the geographic location of recognisable points in the image. Additionally, the code is designed such that the user can enter both minimum and maximum estimates for the horizontal field of view of the camera to facilitate quantification of the uncertainty associated with this parameter. Whilst these are useful techniques, it is always best practice to have accurate and precise metadata.

4.4 An alternative technique: multiple cameras

A number of the uncertainties intrinsic to this method could possibly be addressed by using multiple cameras with different orientations, and applying stereo techniques to construct a 3D model of the plume [e.g. Wood et al. 2019]. Specifically, for optimal camera locations, uncertainty due to alignment of the wind direction and camera orientation could be significantly reduced. 3D properties of the plume, such as volume estimates, could also be estimated since the 2D approximation can be relaxed. However, in order to obtain useful results, the stereo methods will necessarily be accompanied by processing techniques to segment the image [Vulpiani et al. 2016; Bombrun et al. 2018; Wood et al. 2019; Simionato et al. 2022]. One of the benefits of the calibration technique provided here is that it can be applied to user-selected points so, in instances where the quantity of images is not large, can be applied in sub-optimal imaging conditions. Furthermore, it is not always possible to have multiple cameras in optimal locations as part of a field campaign or a monitoring network.

5 CONCLUSIONS

The procedure and method presented in this paper offer a new tool to determine the height and distance from the vent of points within wind-affected volcanic plumes. This could be either tephra (as in the examples shown in this manuscript) or gas plumes. By considering the effect of wind on the calibration of points in images of volcanic plumes, under- or overes-

timation of the height of a volcanic plume can be prevented. The procedure is quick and applicable to any videos of volcanic plumes or, indeed, other types of plumes, e.g. hydrothermal, cooling towers, or smoke from fires. All that is required is knowledge of the camera properties and the location of the vent from which the volcanic plume originates. These values, along with knowledge of how to change input values in a programming script, allow the user to not only determine the height of a point on a volcanic plume, but also its distance from the volcanic vent. Therefore, key characteristics of the volcanic plume can be determined (e.g. plume velocities, shape of the upper and lower plume margins, and radius of the plume).

AUTHOR CONTRIBUTIONS

ES and PAJ developed the methodology presented in this manuscript and wrote the manuscript. ES did the analysis of the volcanic tephra plume from the 12 April 2013 eruption of Mount Etna and PAJ did the analysis of the Vulcanican explosion from Sabancaya volcano. RS provided testing of the methodology. CB, SS, and MP contributed to key discussion on the methodology along with ES and PAJ. All authors read and reviewed the manuscript.

ACKNOWLEDGEMENTS

ES is supported by a NERC GW4+ Doctoral Training Partnership studentship from the Natural Environment Research Council [NE/L002434/1] and is thankful for the support and additional funding from CASE partner, Istituto Nazionale di Geofisica e Vulcanologia, Osservatorio Etneo. The authors would also like to thank Allan Fries for the filming of the Vulcanican explosion from Sabancaya volcano that was examined in this manuscript. We thank also the scientists and technicians from INGV-OE for the camera network maintenance.

DATA AVAILABILITY

The MATLAB version of the code can be found at <https://doi.org/10.5281/zenodo.7812383> and the Python version at <https://doi.org/10.5281/zenodo.7812389>.

COPYRIGHT NOTICE

© The Author(s) 2023. This article is distributed under the terms of the [Creative Commons Attribution 4.0 International License](https://creativecommons.org/licenses/by/4.0/), which permits unrestricted use, distribution, and reproduction in any medium, provided you give appropriate credit to the original author(s) and the source, provide a link to the Creative Commons license, and indicate if changes were made.

REFERENCES

- Berrisford, P., D. Dee, P. Poli, R. Brugge, K. Fielding, M. Fuentes, P. Kallberg, S. Kobayashi, S. S. Uppala, and A. Simmons (2011). *The ERA-Interim archive, version 2.0*. URL: <https://www.ecmwf.int/node/8174> (visited on 09/01/2023).
- Bombrun, M., D. Jessop, A. Harris, and V. Barra (2018). “An algorithm for the detection and characterisation of volcanic plumes using thermal camera imagery”. *Journal of Volcanology and Geothermal Research* 352, pages 26–37. DOI: [10.1016/j.jvolgeores.2018.01.006](https://doi.org/10.1016/j.jvolgeores.2018.01.006).
- Bonadonna, C., A. Folch, S. Loughlin, and H. Puempel (2012). “Future developments in modelling and monitoring of volcanic ash clouds: outcomes from the first IAVCEI-WMO workshop on Ash Dispersal Forecast and Civil Aviation”. *Bulletin of Volcanology* 74, pages 1–10. DOI: [10.1007/s00445-011-0508-6](https://doi.org/10.1007/s00445-011-0508-6).
- Bonadonna, C., M. M. Pistolesi, R. Cioni, W. Degruyter, M. Elissondo, and V. Baumann (2015). “Dynamics of wind-affected volcanic plumes: The example of the 2011 Cordón Caulle eruption, Chile”. *Journal of Geophysical Research: Solid Earth* 120(4), pages 2242–2261. DOI: [10.1002/2014JB011478](https://doi.org/10.1002/2014JB011478).
- Bursik, M. (2001). “Effect of wind on the rise height of volcanic plumes”. *Geophysical Research Letters* 28(18), pages 3621–3624. DOI: [10.1029/2001GL013393](https://doi.org/10.1029/2001GL013393).
- Calvari, S., F. Cannavò, A. Bonaccorso, L. Spampinato, and A. G. Pellegrino (2018). “Paroxysmal Explosions, Lava Fountains and Ash Plumes at Etna Volcano: Eruptive Processes and Hazard Implications”. *Frontiers in Earth Science* 6, page 107. DOI: [10.3389/feart.2018.00107](https://doi.org/10.3389/feart.2018.00107).
- Calvari, S., G. G. Salerno, L. Spampinato, M. Gouhier, A. L. Spina, E. Pecora, A. J. L. Harris, P. Labazuy, E. Biale, and E. Boschi (2011). “An unloading foam model to constrain Etna’s 11-13 January 2011 lava fountaining episode”. *Journal of Geophysical Research: Solid Earth* 116(B11), B11207. DOI: [10.1029/2011JB008407](https://doi.org/10.1029/2011JB008407).
- Cameron, C., S. G. Prejean, M. L. Coombs, K. L. Wallace, J. A. Power, and D. C. Roman (2018). “Alaska Volcano Observatory Alert and Forecasting Timeliness: 1989-2017”. *Frontiers in Earth Science* 6, page 86. DOI: [10.3389/feart.2018.00086](https://doi.org/10.3389/feart.2018.00086).
- Carazzo, G., F. Girault, T. Aubry, H. Bouquerel, and E. Kaminski (2014). “Laboratory experiments of forced plumes in a density-stratified crossflow and implications for volcanic plumes”. *Geophysical Research Letters* 41, pages 8759–8766. DOI: [10.1002/2014GL061887](https://doi.org/10.1002/2014GL061887).
- Coppola, D., S. Valade, P. Masias, M. Laiola, F. Massimetti, A. Campus, R. Aguilar, R. Anccasi, F. Apaza, B. Ccallata, C. Cigolini, L. F. Cruz, A. Finizola, K. Gonzalez, O. Macedo, R. Miranda, M. Ortega, R. Paxi, E. Taipei, and D. Valdivia (2022). “Shallow magma convection evidenced by excess degassing and thermal radiation during the dome-forming Sabancaya eruption (2012-2020)”. *Bulletin of Volcanology* 84, page 16. DOI: [10.1007/s00445-022-01523-1](https://doi.org/10.1007/s00445-022-01523-1).
- Corradini, S., L. Guerrieri, V. Lombardo, L. Merucci, M. Musacchio, M. Prestifilippo, S. Scollo, M. Silvestri, G. Spata, and D. Stelitano (2018). “Proximal Monitoring of the 2011–2015 Etna Lava Fountains Using MSG-SEVIRI Data”. *Geosciences* 8(4), page 140. DOI: [10.3390/geosciences8040140](https://doi.org/10.3390/geosciences8040140).
- Dee, D. P., S. M. Uppala, A. J. Simmons, P. Berrisford, P. Poli, and S. K. et al. (2011). “The ERA-Interim reanalysis: Configuration and performance of the data assimilation system”. *Quarterly Journal of the Royal Meteorological Society* 137(656), pages 553–597. DOI: [10.1002/qj.828](https://doi.org/10.1002/qj.828).
- Degruyter, W. and C. Bonadonna (2012). “Improving on mass flow rate estimates of volcanic eruptions”. *Geophysical Research Letters* 39, page L16308. DOI: [10.1029/2012GL052566](https://doi.org/10.1029/2012GL052566).
- Dioguardi, F., F. Beckett, T. Dürig, and J. A. Stevenson (2020). “The impact of eruption source parameter uncertainties on ash dispersion forecasts during explosive volcanic eruptions”. *Journal of Geophysical Research: Atmospheres* 125, e2020JD032717. DOI: [10.1029/2020JD032717](https://doi.org/10.1029/2020JD032717).
- Dürig, T., M. T. Gudmundsson, T. Ágústsdóttir, T. Högnadóttir, and L. S. Schmidt (2021). “The effect of wind and plume height reconstruction methods on the accuracy of simple plume models - a second look at the 2010 Eyjafjallajökull eruption”. *Bulletin of Volcanology* 84, page 33. DOI: [10.1007/s00445-022-01541-z](https://doi.org/10.1007/s00445-022-01541-z).
- Folch, A. (2012). “A review of tephra transport and dispersal models: Evolution, current status and future perspectives”. *Journal of Volcanology and Geothermal Research* 235–236, pages 66–115. DOI: [10.1016/j.jvolgeores.2012.05.020](https://doi.org/10.1016/j.jvolgeores.2012.05.020).
- Formenti, Y., T. H. Druitt, and K. Kelfoun (2003). “Characterisation of the 1997 Vulcanian explosions of Soufrière Hills Volcano, Montserrat, by video analysis”. *Bulletin of Volcanology* 65, pages 587–605. DOI: [10.1007/s00445-003-0288-8](https://doi.org/10.1007/s00445-003-0288-8).
- Freret-Lorgeril, V., F. Donnadieu, S. Scollo, A. Provost, P. Fréville, Y. Guéhenneux, C. Hervier, M. Prestifilippo, and M. Coltelli (2018). “Mass Eruption Rates of Tephra Plumes During the 2011-2015 Lava Fountain Paroxysms at Mt. Etna From Doppler Radar Retrievals”. *Frontiers in Earth Science* 6, page 73. DOI: [10.3389/feart.2018.00073](https://doi.org/10.3389/feart.2018.00073).
- Harris, A. J. L., D. D. Donne, J. Dehn, M. Ripepe, and A. K. Worden (2013). “Volcanic plume and bomb field masses from thermal infrared camera imagery”. *Earth and Plan-*

- etary Science Letters 365, pages 77–85. DOI: [10.1016/j.epsl.2013.01.004](https://doi.org/10.1016/j.epsl.2013.01.004).
- Hersbach, H., B. Bell, P. Berrisford, S. Hirahara, A. Horányi, J. Muñoz Sabater, J. Nicolas, C. Peubey, R. Radu, D. Schepers, et al. (2020). “The ERA5 global reanalysis”. *Quarterly Journal of the Royal Meteorological Society* 146(730), pages 1999–2049. DOI: [10.1002/qj.3803](https://doi.org/10.1002/qj.3803).
- Hersbach, H., B. Bell, P. Berrisford, G. Biavati, A. Horányi, J. Muñoz Sabater, J. Nicolas, C. Peubey, R. Radu, I. Rozum, D. Schepers, A. Simmons, C. Soci, D. Dee, and J.-N. Thépaut (2018). “ERA5 hourly data on pressure levels from 1979 to present”. Copernicus Climate Change Service (C3S) Climate Data Store (CDS). DOI: [10.24381/cds.bd0915c6](https://doi.org/10.24381/cds.bd0915c6). [Dataset].
- Kern, C., P. Masias, F. Apaza, K. A. Reath, and U. Platt (2017). “Remote measurement of preeruptive water vapor emissions at Sabancaya volcano by passive differential optical absorption spectroscopy”. *Journal of Geophysical Research: Solid Earth* 122(5), pages 3540–3564. DOI: [10.1002/2017JB014020](https://doi.org/10.1002/2017JB014020).
- Manrique Llerena, N., I. A. Lazarte Zerpa, K. A. Cueva Sandoval, S. B. Japura Paredes, and R. Aguilar Contreras (2018). “Actividad del volcan Sabancaya (Peru 2016-2017: observaciones petrograficas y geoquimicas de los depositos de tefras des 2017”. *Hazard and risk mapping: The Arequipa - El Misti case study and other threatened cities*. Edited by J. C. Thouret. Presses universitaires Blaise Pascal, Clermont-Ferrand.
- Miller, C. A. and A. D. Jolly (2014). “A model for developing best practice volcano monitoring: a combined threat assessment, consultation and network effectiveness approach”. *Natural Hazards* 71, pages 493–522. DOI: [10.1007/s11069-013-0928-z](https://doi.org/10.1007/s11069-013-0928-z).
- Patrick, M. R. (2007). “Dynamics of Strombolian ash plumes from thermal video: Motion, morphology, and air entrainment”. *Journal of Geophysical Research: Solid Earth* 112, B06202. DOI: [10.1029/2006JB004387](https://doi.org/10.1029/2006JB004387).
- Sahetapy-Engel, S. T. and A. J. L. Harris (2009). “Thermal-image-derived dynamics of vertical ash plumes at Santiaguito volcano, Guatemala”. *Bulletin of Volcanology* 71, pages 827–830. DOI: [10.1007/s00445-009-0284-8](https://doi.org/10.1007/s00445-009-0284-8).
- Scollo, S., M. Prestifilippo, C. Bonadonna, R. Cioni, S. Corradini, W. Degruyter, E. Rossi, M. Silvestri, E. Biale, G. Carparelli, C. Cassisi, L. Merucci, M. Musacchio, and E. Pecora (2019). “Near-Real-Time Tephra Fallout Assessment at Mt. Etna, Italy”. *Remote Sensing* 11, page 24. DOI: [10.3390/rs11242987](https://doi.org/10.3390/rs11242987).
- Scollo, S., M. Prestifilippo, E. Pecora, S. Corradini, L. Merucci, G. Spata, and M. Coltelli (2014). “Eruption column height estimation of the 2011-2013 Etna lava fountains”. *Annals of Geophysics* 57(2). DOI: [10.4401/ag-6396](https://doi.org/10.4401/ag-6396).
- Simionato, R., P. A. Jarvis, E. Rossi, and C. Bonadonna (2022). “PlumeTraP: A New MATLAB-Based Algorithm to Detect and Parametrize Volcanic Plumes from Visible-Wavelength Images”. *Remote Sensing* 14(7), page 1766. DOI: [10.3390/rs14071766](https://doi.org/10.3390/rs14071766).
- Snee, E. (2021). “Volcanic plumes from explosive basaltic eruptions: the case of Mount Etna (Italy)”. PhD thesis. Cardiff University.
- Sparks, R. S. J. and L. Wilson (1982). “Explosive volcanic eruptions - V. Observations of plume dynamics during the 1979 Soufrière eruption, St Vincent”. *Geophysical Journal International* 69(2), pages 551–570. DOI: [10.1111/j.1365-246X.1982.tb04965.x](https://doi.org/10.1111/j.1365-246X.1982.tb04965.x).
- Suwa, H., Y. J. Suzuki, and A. Yokoo (2014). “Estimation of exit velocity of volcanic plume from analysis of vortex structures”. *Earth and Planetary Science Letters* 385, pages 154–161. DOI: [10.1016/j.epsl.2013.10.032](https://doi.org/10.1016/j.epsl.2013.10.032).
- Terada, A. and Y. Ida (2007). “Kinematic features of isolated volcanic clouds revealed by video records”. *Geophysical Research Letters* 34, page L01305. DOI: [10.1029/2006GL026827](https://doi.org/10.1029/2006GL026827).
- Tournigand, P., J. Taddeucci, D. Gaudin, J. J. P. Fernández, E. D. Bello, P. Scarlato, U. Keuppens, J. Sesterhenn, and A. Yokoo (2017). “The Initial Development of Transient Volcanic Plumes as a Function of Source Conditions”. *Journal of Geophysical Research: Solid Earth* 112, pages 9784–9803. DOI: [10.1002/2017JB014907](https://doi.org/10.1002/2017JB014907).
- Vulpiani, G., M. Ripepe, and S. Valade (2016). “Mass discharge rate retrieval combining weather radar and thermal camera observations”. *Journal of Geophysical Research: Solid Earth* 121(8), pages 5679–5695. DOI: [10.1002/2016JB013191](https://doi.org/10.1002/2016JB013191).
- Webb, E. B., N. R. Varley, D. M. Pyle, and T. A. Mather (2014). “Thermal imaging and analysis of short-lived Vulcanian explosions at Volcán de Colima, Mexico”. *Journal of Volcanology and Geothermal Research* 278-279, pages 132–145. DOI: [10.1016/j.jvolgeores.2014.03.013](https://doi.org/10.1016/j.jvolgeores.2014.03.013).
- Wood, K., H. Thomas, M. Watson, A. Calway, T. Richardson, K. Stebel, A. Naismith, L. Berthoud, and J. Lucas (2019). “Measurement of three dimensional volcanic plume properties using multiple ground based infrared cameras”. *ISPRS Journal of Photogrammetry and Remote Sensing* 154, pages 163–175. DOI: [10.1016/j.isprsjprs.2019.06.002](https://doi.org/10.1016/j.isprsjprs.2019.06.002).

APPENDIX A

Estimation of θ_H for the camera calibration

The horizontal field of view θ_H is a crucial parameter to be able to calibrate any images. As this value was unavailable for the videos presented in this study, we estimated the values by using Google Earth. First, a horizontal line is drawn in Google Earth from the camera location along the horizontal projection of the centreline of the image (i.e. the LOS). For the Mount Etna case-study, this connects the camera position with the summit crater area of Mount Etna (i.e. a recognisable point), which is in the horizontal centre of the FOV. A vertical plane, that is perpendicular to this line and goes through the region of interest (i.e. the South East Crater (SEC) for Mount Etna and the summit crater for Sabancaya), can then be drawn (i.e. the image plane). By positioning oneself at the camera location within Google Earth and adjusting the view to be similar to the one in the videos, it is possible to estimate and mark the right-and/or left-hand margins of the video. A line, or lines can then be drawn connecting this/these point(s) and the camera



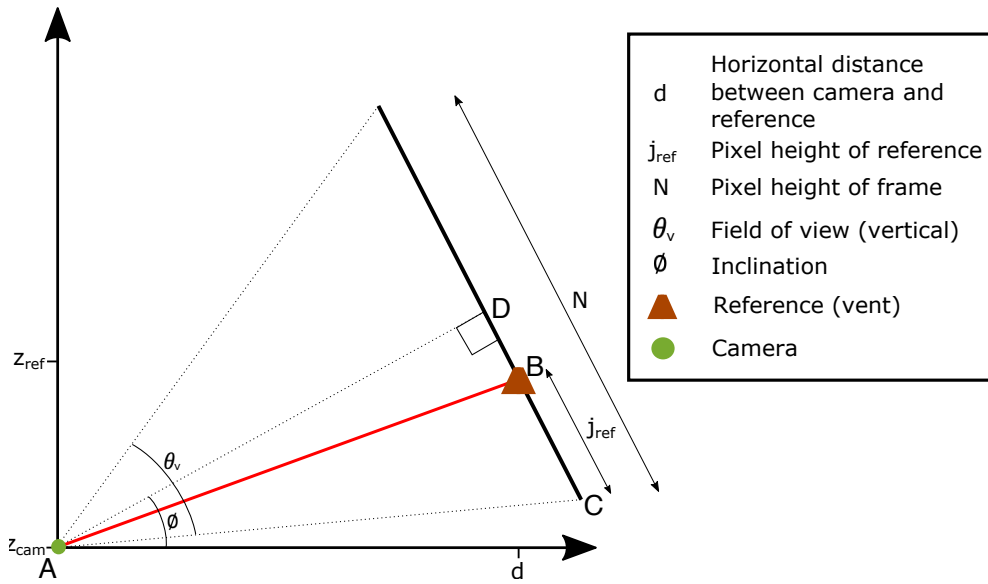


Figure A1: Diagram defining the length scales and angles used to calculate the camera inclination.

position. The angle this/these lines makes with the horizontal projection of the centreline is equal to $\theta_h/2$. Therefore, θ_h is calculated by doubling this calculated value. However, for the video in the presented Etna case-study, the image frame margins do not intersect with the slope of the volcano. This makes it difficult to precisely determine θ_h . However, it is possible to constrain the minimum value to be 16° . Given the uncertainty on this value though, the value of θ_h for the ECV camera is allowed to vary. Given that the INGV-OE has a calibration for the ECV camera only, it is possible to compare results with the calibration procedure described here with that used operationally. Best agreement between the two procedures is obtained for $\theta_h = 18^\circ$. We therefore choose to use the value of $\theta_h = 18^\circ$ for the ECV camera calibration case-study. This difficulty is not present in the Sabancaya case, where the video edges intersect with mountaneous topography. Consequently, for Sabancaya, it was straightforward to identify that $\theta_h = 64^\circ$.

Estimation of the camera inclination

If the camera inclination ϕ is unknown, such as for the Mt. Etna case study in Section 3.2, it can be estimated from the camera field of view, pixel dimensions of the image frame and a known reference point. Figure A1 shows the set-up for inclination derivation using these known values.

First, ψ can be defined as the angle denoted by the line between the camera (A) and the reference point (B) and the horizontal. It can be calculated as

$$\psi = \tan^{-1} \left(\frac{z_{ref} - z_{cam}}{d'} \right), \quad (7)$$

where d' is the horizontal distance between the camera and the reference point in the image frame. The angles denoted by BAC and ACB (see Figure A1), where C in the lowest vertical point in the image frame, can then be defined as $\theta_v/2 - (\phi - \psi)$ and $90 - \theta_v/2$, respectively. Using these angles in the sine rule allows the length AB to be defined as

$$AB = \cos \left(\frac{\theta_v}{2} \right) \left[\sin \left(\frac{\theta_v}{2} - (\phi - \psi) \right) \right]^{-1} j_{ref}. \quad (8)$$

However, as there are multiple unknown terms in this equation, we need another expression for AB to be able to determine the value of ϕ . By defining the angle DAB, where D defines the vertical midpoint in the image frame, as

$$DAB = \phi - \psi, \quad (9)$$

and the length DB as

$$DB = \frac{N}{2} - j_{ref}, \quad (10)$$

the length AB can also be written as

$$AB = \frac{\frac{N}{2} - j_{ref}}{\sin(\phi - \psi)}, \quad (11)$$

and rearranged to be

$$AB = \frac{N - 2j_{ref}}{2 \sin(\phi - \psi)}. \quad (12)$$

Equations 8 and 12 can now be set equal to each other as

$$\cos \left(\frac{\theta_v}{2} \right) \left[\sin \left(\frac{\theta_v}{2} - (\phi - \psi) \right) \right]^{-1} j_{ref} = \frac{N - 2j_{ref}}{2 \sin(\phi - \psi)}, \quad (13)$$

which can be rearranged to determine ϕ

$$\phi = \tan^{-1} \left(\frac{z_{ref} - z_{cam}}{d'} \right) + \tan^{-1} \left[\left(1 - \frac{2j_{ref}}{N} \right) \tan \left(\frac{\theta_v}{2} \right) \right]. \quad (14)$$